

Innovative tensile test for brittle materials: Validation on graphite R4550

*Original*

Innovative tensile test for brittle materials: Validation on graphite R4550 / Pagnoncelli, A. P.; Paolino, D. S.; Peroni, L.; Tridello, A.. - In: INTERNATIONAL JOURNAL OF MECHANICAL SCIENCES. - ISSN 0020-7403. - 261:1(2024).  
[10.1016/j.ijmecsci.2023.108679]

*Availability:*

This version is available at: 11583/2987731 since: 2024-04-11T12:32:53Z

*Publisher:*

PERGAMON-ELSEVIER SCIENCE LTD

*Published*

DOI:10.1016/j.ijmecsci.2023.108679

*Terms of use:*

This article is made available under terms and conditions as specified in the corresponding bibliographic description in the repository

*Publisher copyright*

(Article begins on next page)



# Innovative tensile test for brittle materials: Validation on graphite R4550

A.P. Pagnoncelli<sup>\*</sup>, D.S. Paolino, L. Peroni, A. Tridello

Department of Mechanical and Aerospace Engineering, Politecnico di Torino, Turin 10129, Italy

## ARTICLE INFO

### Keywords:

Ultrasonic tensile test  
Tensile strength  
Numerical model optimization  
Graphite R4550

## ABSTRACT

This paper proposes an innovative ultrasonic tensile test methodology for the assessment of quasi-static uniaxial mechanical properties and tensile strength of brittle materials. An ultrasonic testing machine, commonly employed for very high cycle fatigue tests, had its control and data acquisition systems adapted to induce specimen failure in about 100 cycles, avoiding cyclic load damage. The mechanical properties are thereafter estimated with a finite element model which simulates the experimental test. The proposed method has been validated by assessing the tensile strength of graphite R4550, characterized by brittle behaviour. The mechanical properties for graphite R4550 estimated with this experimental-numerical approach were found to be close to literature values obtained in different quasi-static testing configurations, confirming the effectiveness of the proposed method and the feasibility of employing the ultrasonic fatigue testing machine for studying the behaviour of brittle materials. Furthermore, the proposed methodology eliminated issues caused by mechanical fixtures and tensile testing machine alignment, while also allowing a considerable increase of the material loaded volume when compared to that of traditional test methods. The experimental and numerical approaches are successfully validated on graphite R4550, also highlighting its capability of characterizing the material nonlinear behaviour, including viscoelasticity and asymmetrical response in tension and compression.

## 1. Introduction

The difficulties generally encountered in mechanical testing of brittle materials, e.g., fixture failures and machine alignment [1,2], which invalidate the experimental test, have forced researchers to develop new experimental methods. Furthermore, the lack of evidence of nearing their mechanical limits – such as low fracture strains, a general absence of plasticity, and low fracture toughness – is often responsible for their catastrophic failures [3,4], requiring a sounder knowledge of these materials behaviour.

The above-mentioned issues in testing brittle materials also limit the types of mechanical tests that can be successfully employed for the assessment of their mechanical properties, with the majority of test methods developed to avoid the use of mechanical fixtures, which often induce premature failure on the clamped zones of the specimen, and to reduce the precision required for testing machine alignment, which is the more critical the lower the material fracture strain. Particularly three and four-point bending are amongst the most widespread tests for brittle materials, from glass to concrete to advanced ceramics, since they do not require a precise machine alignment or critical clamping of the specimen, tested with simple geometries, such as bars, plates and rods [5–9],

but also with more complex shapes, as in [10] and [11].

Other types of tests that avoid the necessity of mechanical grips are also employed, with many of them generating multiaxial stress states. This is the case for ring-on-ring and ASTM C1550, and their variations as in [12] and [13], which require specimens with a simple disc geometry. Similarly, the Brazilian splitting test [14] is also widely employed, as well as other tests that apply compressive loads on the specimen, aiming to generate a multiaxial stress state [15], allowing to test both simple specimen geometries, such as discs [16,17], spheres [18], and rings [19], as well as more particular geometries [20–22]. Additionally, less traditional experimental procedures have been found in the literature, such as the ring hoop tension test [23], the wedge splitting test [24], the Iosipescu test method [25] (usually employed to characterize shear strain behaviour of composite materials), or a tensile testing apparatus that uses tubular specimens [26].

In general, these methods can be applied to test brittle materials such as concrete [27,28], glass [29], graphite [19], composites [30], and advanced ceramics, like silicon carbide [31], alumina [32], and silicon nitride [18]. Moreover, the literature shows experimental results for most of the above-mentioned test configurations at different strain rates [29,33–35], including impact tests on split Hopkinson pressure bar [36,

<sup>\*</sup> Corresponding author.

E-mail address: [ana.pagnoncelli@polito.it](mailto:ana.pagnoncelli@polito.it) (A.P. Pagnoncelli).

<https://doi.org/10.1016/j.ijmecsci.2023.108679>

Received 24 May 2023; Received in revised form 18 July 2023; Accepted 10 August 2023

Available online 13 August 2023

0020-7403/© 2023 The Authors. Published by Elsevier Ltd. This is an open access article under the CC BY license (<http://creativecommons.org/licenses/by/4.0/>).

37].

However, the previously described tests often require the indirect calculation of the material tensile strength from the induced multiaxial stress state, while usually being limited to relatively low loaded volume, which corresponds to the material volume subjected to a stress close to the maximum applied stress. Indeed, the strength of brittle materials is strongly affected by defects and their size [38,39]. The defect size is dependant on the material loaded volume, i.e., large defects are statistically more likely to occur in large material volumes, with a consequent decrease of the part strength [27,40,41]. For this reason, it is important to test specimens characterized by loaded volumes as large as possible, in order to properly and reliably account for the influence on the mechanical strength of size effect associated with defect size.

Furthermore, the objective of mechanical tests on brittle materials is the assessment of their tensile strength, since their low fracture toughness and, consequently, high susceptibility to defects, implies that the most critical type of stress for these materials is the tensile stress that induces crack opening [42], following Irwin's definition of fracture mode I [43]. For this reason, testing configurations have also been developed to directly measure the mechanical tensile behaviour of brittle materials. However, they frequently require specific specimen geometries [44], being often only applicable to low-strength materials [45,46], or still resulting in very small loaded volumes of high-strength materials [47–50].

Therefore, aiming for a more direct calculation of tensile strength than that of biaxial or multiaxial tests, while also eliminating the mechanical fixtures and testing machine alignment issues, and potentially allowing for larger flexibility on the choice of the loaded volume, a novel test method is developed in the present paper, being referred to as Ultrasonic Tensile (UST) test. The UST test method employs an ultrasonic testing machine, commonly used for Very High Cycle Fatigue (VHCF) tests on metallic materials. Accordingly, with the proposed testing configuration, fatigue damage mechanisms are eliminated, or at least minimized, with negligible influence [51], with the assessed material strength being thus expected to be close to the one measured through a conventional quasi-static tensile test [52], or even values calculated in biaxial and multiaxial tests.

During the UST test, the displacement curves over time of multiple points of the specimen until its failure are acquired. The experimentally measured displacements are then considered in a Finite Element Model (FEM) of the test, optimized to obtain the material behaviour model and its respective properties values that should reproduce the specimen experimental displacement curves. Once the FEM is optimized, the tensile strength of each specimen, corresponding to the maximum stress achieved at fracture, is obtained.

The proposed experimental and numerical methodology is performed on graphite R4550, artificially produced by compressing the raw material mixture into rectangular or round blocks using a cold isostatic press, tendentially resulting in the smallest grain sizes amongst graphites and conferring it higher mechanical resistance [53]. As one of the materials employed in Large Hadron Collider collimators [54,55], it has high thermal shock resistance and is very easy to machine, allowing some level of freedom in the choice of specimen geometry. Although R4550 is characterized by isotropic properties, it is also expected to behave nonlinearly as often observed in graphene-based materials [56–59].

## 2. Experimental procedure

Ultrasonic fatigue tests were developed to characterize the fatigue response of materials used in structural components with very large fatigue lives (up to  $10^{10}$  cycles) [60], such as those experienced by automotive, aerospace, and railway components. In standard ultrasonic fatigue tests, the specimen works in resonance conditions in a range of loading frequency close to 20kHz (ultrasound), allowing a considerable reduction of testing time.

According to [61], although ultrasonic fatigue testing machines that could operate at higher frequencies were designed over the years, the further reduction in testing time does not ensure significant advantages, while, on the other hand, they are counterbalanced by more pronounced disadvantages, such as the reduction of test measurement accuracy, and increased difficulty in the design of the specimens and of the vibrating components, e.g., the horn and the booster. Moreover, for this innovative testing configuration, the reduction of the testing time is not an objective, since the test ends in less than 10 milliseconds. Nevertheless, exploiting the resonance condition, necessary for running experimental tests at ultrasonic frequencies, allows to avoid the use of mechanical clamping systems, since the specimen is attached to the horn with an adhesively bonded butt-joint. Indeed, by considering the stress distribution along the vibrating components and the specimen length, the adhesive joint is located at a stress node, i.e., the adhesive is subjected to a stress amplitude close to zero. This prevents failures in the clamping region, which can occur when traditional tensile tests on brittle materials are carried out, invalidating the test results, representing one of the main drawbacks. Secondly, bending spurious stresses that can be induced when the specimen is clamped in traditional testing systems are avoided, since the specimen is bonded at one end and free at the other. While this method was initially applied to uniaxial fatigue tests (tension-compression), over the last decade, new configurations for fatigue tests using the ultrasonic machine have been proposed, including bending, torsion, multiaxial tension-compression and torsion, and in-plane biaxial stress [62].

This flexibility of the ultrasonic equipment has allowed the development of the UST method. While using the same device configuration as the one applied to tension-compression VHCF tests, the test proposed in the present paper is designed to reach the material ultimate stress in a limited number of cycles – the minimum number allowable by the equipment – avoiding fatigue damage mechanisms. Moreover, since brittle materials have considerably lower resistance in tension than in compression, it is expected that the tensile stress will be the one causing the specimen damage and failure, hence the name ultrasonic tensile even though an alternating tension and compression load is applied.

### 2.1. UST testing equipment description

The ultrasonic testing machine is capable of operating in a frequency range between 19.5kHz and 20.5kHz, and its main components are an ultrasonic generator, a piezoelectric transducer, and a booster, all provided by Branson Ultrasonics. A second mechanical amplifier, the horn, is rigidly connected to the booster with a threaded connection to further amplify the displacement in output from the booster. The horn, indeed, ensures the displacement amplification allowing to apply the required stress at the specimen centre. Finally, two devices for measuring the specimen displacement are used, i.e., a laser and a high-speed camera, as well as strain gauges placed on the horn to verify the machine output, all of which are described in detail in SubSection 3.3. All the mentioned components are indicated in Fig. 1a, representing the configuration of the machine in Fig. 1b.

This equipment configuration provides an imposed displacement amplitude at horn-specimen interface in the range  $13.2\mu\text{m}$  -  $120.0\mu\text{m}$ , depending on the displacement amplitude provided in output by the piezoelectric transducer, which is controlled by an external control system. The ramp time is equal to 10ms. The ramp is defined as the period between the start of the test, when the longitudinal vibration starts, and the time when the imposed amplitude output is reached. At the end of the ramp the specimen vibrates at constant amplitude, i.e., in regime condition. Given the device operating frequency, the ramp is expected to last for around 200cycles, meaning that the specimen is likely to fail while the vibration amplitude is still increasing. Therefore, the machine output regime amplitude, is set as well above the estimated value capable of producing the specimen ultimate stress.

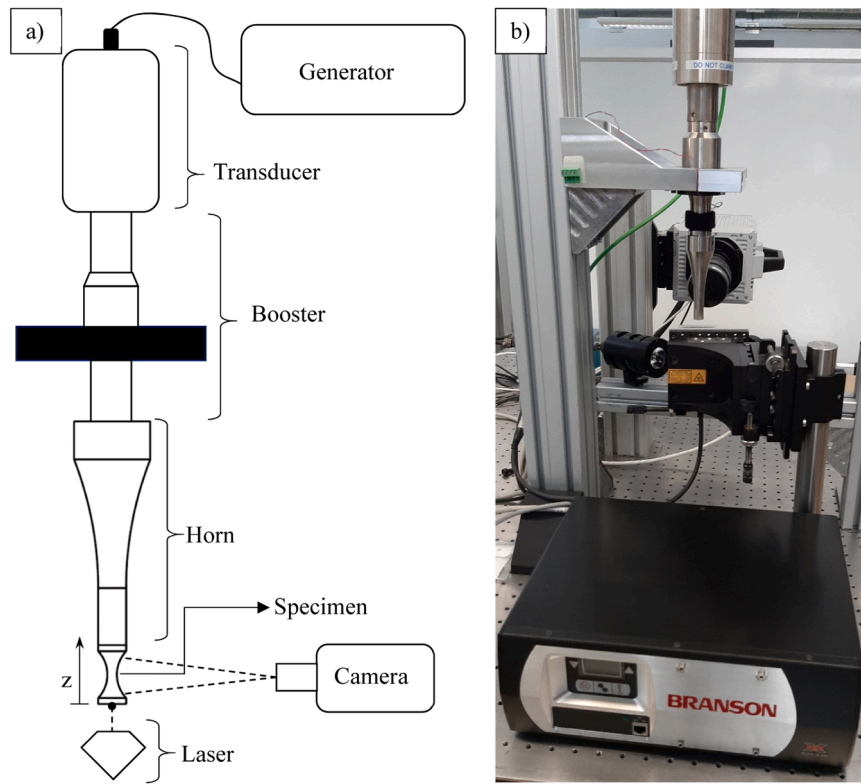


Fig. 1. Ultrasonic testing machine: (a) diagram indicating its main components, and (b) the apparatus used in this paper.

## 2.2. Specimen design

Taking advantage of graphite R4550 high machinability, a characteristic rarely found in brittle materials, the specimens were designed with hourglass geometry and circular cross-section, using a linear-elastic material FEM in Ansys Workbench, assuming a density of  $1860\text{kg/m}^3$  and an elastic modulus of  $10.9\text{GPa}$ , values derived from measurements conducted on graphite R4550 bars, specifically, their mass, dimensions and natural frequency through Impulse Excitation Technique (IET). The specimen was designed in order to have the first longitudinal resonance mode at  $20\text{kHz}$ , with the expected tensile strength at the specimen centre achievable for the range of displacement amplitude imposed by the piezoelectric transducer. The normal stress amplitude distribution in regime condition for an applied displacement amplitude at the horn-specimen interface, referred to as  $A_{out}$ , equal to  $120.0\mu\text{m}$  is shown in Fig. 2, along with the specimen geometry.

Since 4-point bending tests on this graphite provide a failure strength of  $61.2\text{MPa}$  [63], and setting  $A_{out} = 48\mu\text{m}$  in the UST test provides  $80\text{MPa}$  of maximum stress at the end of the ramp, the specimen should undergo failure during the ramp while also avoiding issues caused by large strain rates.

Additionally, the ultrasonic machine limit consists of a displacement amplitude, instead of a load as in quasi-static testing machines. Hence, materials with large elastic moduli, such as advanced ceramics, should undergo proportionally larger stress levels when in resonance, possibly allowing simpler specimen geometries to be designed, such as rectangular cross-section with hourglass or dog-bone profiles (flat instead of round as the one in Fig. 2), or even constant cross-section specimens, such as bars and rods.

## 2.3. Measuring devices

The displacements in the longitudinal direction, corresponding to the vertical axis, are acquired through an LK-G5001P laser from Keyence Corporation, using a  $392\text{kHz}$  sampling rate, and a FASTCAM SA5 high-

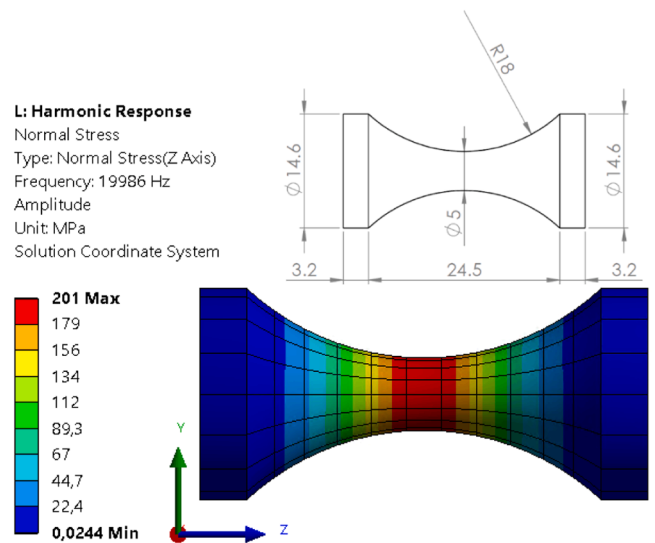


Fig. 2. Graphite specimen geometry (in [mm]), with numerically estimated stress amplitude distribution (in [MPa]), for  $A_{out} = 120\mu\text{m}$ .

speed camera from Photron, with an acquisition rate of  $420\text{kfps}$  with size  $24 \times 512\text{pixels}$ . While the laser measures the displacements at the specimen free extremity, the camera recording window is symmetrically centred along the specimen lateral surface, being expected to capture the fracture position, which should happen near the specimen centre, i. e., in the zone with higher local stress, as shown in Fig. 2.

Moreover, two strain gauges are placed on the horn, both on the zone with higher strain amplitude to reduce the influence of measurement errors caused by noise. Their signal is acquired at a rate of  $2\text{MHz}$ , and given the horn linear-elastic behaviour and the relationship between its strain and displacement, the strain gauges provide the longitudinal

displacement curve at the horn-specimen interface. Fig. 3 shows the schematics of the horn-specimen system, with the specimen following the design model described in SubSection 2.2, and the respective curves showing the behaviour of the longitudinal displacement and strain amplitudes, used to define the positions of the three measuring devices. The camera recording window represents an approximate longitudinal length of 13.9mm.

The camera frames are analysed with the Digital Image Correlation (DIC) technique, using the software DICe, specifically the tracking analysis mode, identifying the displacements along the longitudinal direction from multiple points of the specimen lateral surface. Once all the collected data is synchronized, a preliminary analysis allows to count the number of cycles until failure, as well as the displacement curves over time in correspondence to the laser and the tracking points on the recorded images.

### 3. Numerical procedure

Once the UST test raw data is processed and analysed, the next step for the material characterization can be pursued, i.e., the development of a FEM simulating the experimental test. The material properties which allow to reproduce the measured displacements are obtained through an optimization process. This procedure can be subdivided into 3 main steps:

- FEM setup, comprising the definition of boundary conditions and a material model for the specimen on LS-DYNA after qualitative observation of the experimental displacement behaviour;
- the determination of the optimization variables and objectives in LS-OPT;
- the extraction of the specimen stresses and strains in each finite element once the material properties are optimized, to obtain the maximum achieved normal stress at failure, corresponding to the graphite tensile strength.

#### 3.1. FEM definition

Since the horn was designed to behave linear-elastically within the entire range of the machine amplitude outputs, it was not included in the FEM, in which only the specimen will be involved and analysed. Moreover, given that the specimen geometry is simple, and optimization of material parameters is required, plane elements were selected to model it, which significantly lowers computational time. Specifically, given the specimen circular cross-sections, the axisymmetric formulation was applied.

The boundary conditions were thereafter set. One of the specimen

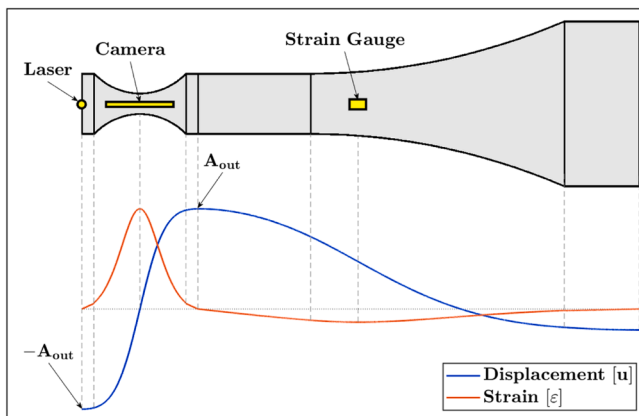


Fig. 3. Schematic of the horn-specimen system indicating the positioning of the measuring devices.

extremities is free, while the other, at the horn-specimen interface, receives the experimental displacement curve over time, i.e., the joined surface displacement ramping up to the set output amplitude, here referred to as the boundary motion curve. This setup can be visualized in Fig. 4a through the LS-DYNA model of the hourglass graphite specimens with the boundary motion curve  $g(t)$ , defining the displacement at the horn-specimen interface nodes, being illustrated through Fig. 4b reporting the experimentally calculated curve for specimen number 16.

The boundary motion curve  $g(t)$  is calculated through the fitting of experimental data measured by the strain gauges. For all the conducted experiments,  $g(t)$  has a form that can be fitted by the equation:

$$g(t) = (at^2 + bt + c) \cdot \sin(2\pi f_{out} \cdot t) \quad (1)$$

being  $f_{out}$  the output frequency of the ultrasonic generator,  $t$  the time from the start of the test, and  $a$ ,  $b$  and  $c$  empirical parameters resulting from the fitting of strain gauges data, then converted into a displacement curve. This allows the elimination of measurement noise, which was observed to introduce instabilities into the numerical model despite the attempts of filtering the data. Instead, the boundary motion curve possesses the smoothness of a sinusoidal function, whose amplitude increases according to the experimentally measured values from the ramp envelope, which can be represented by a parabolic function.

Hence, the main characteristics of the FEM generated in LS-DYNA can be summarized as follows:

- Specimen: simulated with the meshed geometry in Fig. 4a, using plane elements (SHELL) with axisymmetric formulation;
- Boundary conditions: application of a boundary prescribed longitudinal displacement defined by curve  $g(t)$  on all nodes located on the horn-specimen interface;
- Analysis method: transient explicit without added mass, with termination time equal to the maximum time of each respective specimen  $g(t)$ .

#### 3.2. Material properties optimization

The optimization of the material properties is carried out with LS-OPT. The variables to be optimized include one or more of the selected material model properties. The material model is selected through the observation, qualitative characterization, and preliminary FEM simulations before proceeding to optimization.

The optimization objective is the assessment of the material parameters that best reproduce the displacements experimentally measured with the camera and the laser. Therefore, the goal is to minimize the error between the measured displacement and the displacement of the FEM nodes at the corresponding location. Particularly, only the experimental displacements from the last two cycles of valid curves are considered as optimization objectives, since the cycles

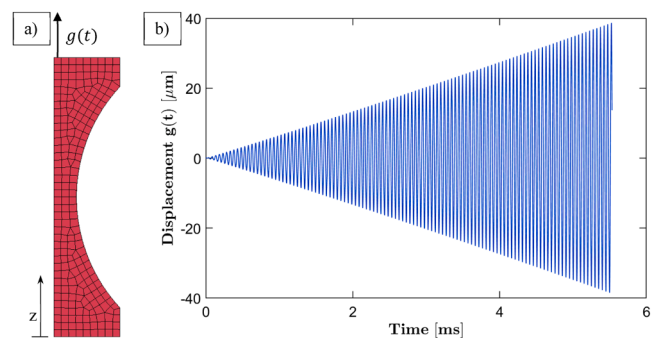


Fig. 4. FEM model of the UST tests on graphite representing (a) the meshed specimen with the boundary conditions, and (b) the displacement curve applied at the horn-specimen interface (the boundary motion curve) of specimen 16.



preceding failure are the ones determining the material strength.

The displacements of the 20 camera tracker points have been linearly interpolated to calculate the experimental displacements at the corresponding nodes of the FEM, being the curves affected by poor local spray-painting job considered non-valid and eliminated from the process. The interpolation is represented in the schematics of Fig. 5a, highlighting where three of the FEM nodes are positioned in the zone recorded by the camera and relative to the tracker selected region of interest (the green squares).

Meanwhile, the optimization setup in LS-OPT is shown in the flux diagram in Fig. 5b, adopting the metamodel-based strategy with domain reduction and the genetic algorithm. The initial values of the 4 optimization variables and their ranges are defined at the beginning, which will be further discussed in Section 4. In each iteration, LS-OPT calculates the FEM results for multiple sets of optimization variables. Afterwards, the minimum square error between the experimental displacements and the values obtained through the numerical simulation is computed for each set. For the subsequent iteration, new sets of variables are selected by LS-OPT, whose objective is the minimization of the minimum square error between the numerical and experimental displacement curves. Once either convergence or the maximum defined number of iterations, in this case 30, is reached, the optimization ends.

### 3.3. Results extraction and analysis

To verify the calculated material properties, the optimized FEM displacements are compared to those experimentally measured by computing the coefficient of determination, according to Eq. (2):

$$R^2 = 1 - \frac{\sum (u_{exp} - u_{num})^2}{\sum (u_{exp} - \bar{u}_{exp})^2} \quad (2)$$

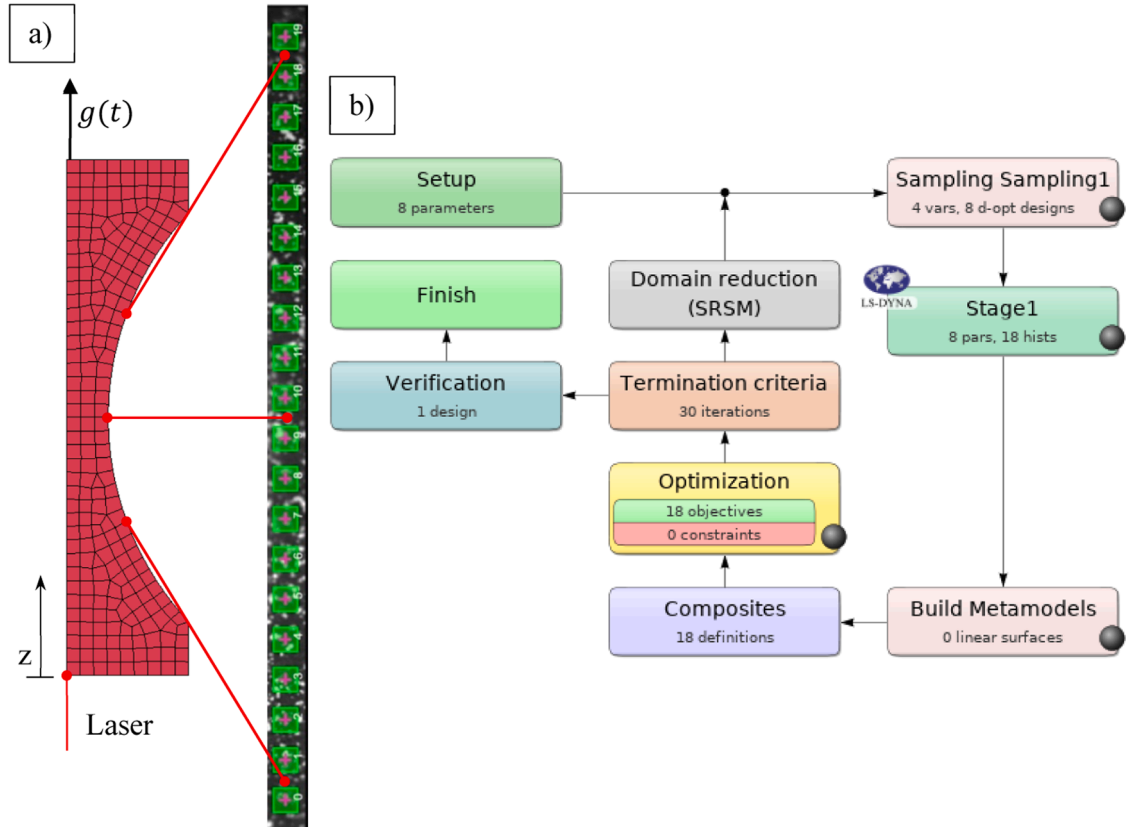


Fig. 5. Definition of the optimization process with (a) the illustration of the interpolation procedure to define the experimental z-displacements of the FEM nodes, added as objectives in (b) the LS-OPT variable optimization flux diagram.

being  $u_{exp}$  and  $u_{num}$  the experimental and the numerical displacement, respectively, at the corresponding FEM node. All the valid displacement curves of the last 20 cycles for each test are considered in Eq. (2), which allows an ample validation of the optimized FEM material, expected to reproduce all the experimental behaviour despite the restricted selection of data as optimization objectives, which would also be an indication of the process robustness.

With the FEM optimized and validated, the normal stress generated in each element can be extracted, particularly the values for the highest global tensile stress achieved on that specimen, referred to as  $\sigma_{max}$ . This quantity, identified as tensile strength, along with the estimated material properties are the final values.

## 4. Results and discussions

The measured specimen density is reported in Table 1 together with the specimen longitudinal natural frequency, measured through IET. The average resonance frequency is 20,971 Hz, which could represent an issue since it is outside the machine operating range. However, ultrasonic tests can be reliably carried out if the horn-specimen system resonance frequency is within the 19,450 Hz – 20,450 Hz range. Since the horn has a mass considerably larger than the mass of the specimen, the resonance frequency of the vibrating system is close to that of the

Table 1  
Preliminary characterization of graphite specimens.

Property	Mean	Standard deviation
Density [ $\frac{kg}{m^3}$ ]	1830	5
Frequency [Hz]	20,971	27

horn. Therefore, UST tests can be carried out for this material.

The elastic modulus, considering a linear-elastic material, was also numerically estimated through Ansys Workbench harmonic response analysis, providing a value of 11.8GPa, larger than the 10.9GPa used for the design. With the resulting density being similar to the one originally employed, the variation in elastic modulus is the reason for the unexpectedly high natural frequency.

Furthermore, due to the larger experimental elastic modulus, the maximum stress at the specimen centre for a displacement amplitude output  $A_{out} = 48\mu\text{m}$  at the horn-specimen interface has been computed again and updated to 97MPa. The final test parameters for the graphite specimens are reported in Table 2, with the output frequency being the mean value measured for the horn-specimen system for each tested specimen.

In particular, according to Table 2, the horn-specimen system had natural frequencies always within the ultrasonic machine output range as expected, making it possible to run the tests.

#### 4.1. UST results

Through the analysis of the camera recordings, it was determined that the adhesive joint at the horn-specimen interface lasted at least until specimen failure in all tests. The displacement along the z-direction for each point acquired by the camera is plotted in Fig. 6 for specimen 16, which is amongst the specimens whose tracker curves were all considered valid. The legend shows the points whose displacements were computed on the recorded frame, also corresponding to the positions of the FEM nodes.

If the specimen were to be considered linear-elastic, while in resonance, the displacement curves should be symmetrical with respect to the abscissa zero, with curve number 9 at constant zero amplitude corresponding to the displacement node, while the points on one side of it would be in counterphase with those on the other side. Therefore, the primary inference drawn from Fig. 6, being supported by the laser measurements provided later in this Subsection, is that graphite R4550 is a nonlinear material, accordingly with literature data on graphene-based materials. The analysis of Fig. 6 showed that graphite R4550 is a viscoelastic material with different elastic moduli in tension and compression respectively, considering the strain range generated in the UST test. The reasoning behind this deduction is detailed in this Subsection.

Firstly, to highlight the difference in behaviour between the initially simulated linear-elastic model for graphite R4550, employed during the specimen design step from SubSection 2.2, and the nonlinear material model selected to describe the experimental behaviour of those same specimens during the UST test, the graphics on Fig. 7 were plotted. These two models are illustrated through longitudinal displacement and strain curves, respectively normalized in each case by  $A_{out,1}$ , the displacement amplitude output at the horn-specimen interface corresponding to the regime amplitude of the conducted tests, and  $\varepsilon_{max,1}$ , the maximum strain amplitude for the linear-elastic model. The nonlinear model, selected and optimized according to the experimental data acquired in the present work, considers two different amplitude outputs,  $A_{out,2}$  and  $A_{out,3}$ . All three cases consider the strain and displacement on the specimen at the instant when  $u = A_{out}$  at the horn-specimen interface. While, in the linear-elastic model the normalized curves are independent from  $A_{out}$ , in the nonlinear model, increasing  $A_{out}$  brings the point with  $u = 0$  closer to the horn-specimen interface and increases the ratio between the value of  $|u|$  on the free surface and  $A_{out}$ .

**Table 2**  
UST test parameters.

Mean output frequency $f_{out}$ [Hz]	Output regime amplitude $A_{out}$ [ $\mu\text{m}$ ]	Maximum stress [MPa]
20,223	48	97

Moreover, the displacement node cannot be observed, originally expected to be in correspondence to point 9. Meanwhile, the tests showed the lowest displacement amplitude around point 8, without any indication of the presence of the displacement node, since, as in Fig. 6, the curves seem to have slightly different phases from one another, with curves 1 and 17 being almost in counterphase. The behaviour concerning both the phases and the lack of a displacement node was confirmed to be replicable through the preliminary use of a linear viscoelastic material model to simulate graphite R4550, since the added time-dependant strain response, causes hysteresis, creep, and stress relaxation, disposing the phases of the displacement curves as in Fig. 6.

Furthermore, alternated tension and compression are applied to the specimen in ultrasonic tests. This can be noticed in Fig. 6 through points 1 and 17, symmetrically positioned with respect to the specimen centre. In the instant when the former assumes a negative displacement and the latter a positive one, the specimen is in tension, when the reverse happens, compression is applied. From this observation, it is established that the specimen in Fig. 6 fails while being submitted to tension, which is also the case for all tested specimens. Moreover, the difference in displacement between these two points is larger in tension than in compression, which is unexpected since the defined boundary motion curve  $g(t)$ , as seen in Fig. 4, is always symmetric with respect to the abscissa zero, meaning that the machine is exerting roughly the same displacement within the same cycle and, consequently, the same load in both tension and compression. Hence, if the same load is causing larger displacements in tension than in compression, it likely means that R4550 has a smaller elastic modulus in tension than in compression.

Finally, still observing the curve evolution shown in Fig. 6, as the test progresses, it can be noticed that the curves do not actually have an axis of symmetry, contrary to the boundary motion curve presented in Fig. 4, since they seem to be displaced downwards as their amplitudes increase. Fig. 6 suggests that the axis of symmetry of the curves is at  $0\mu\text{m}$  for the range  $[0, 0.051]\text{ms}$ , and is progressively decreasing to around  $-5\mu\text{m}$  for the range  $[5.390, 5.456]\text{ms}$ . This specific phenomenon was verified to be a combination of the two previously identified material behaviours of graphite R4550, i.e., viscoelasticity and the asymmetric tension-compression elastic moduli. While either material model by itself was observed to produce curves symmetric with respect to the zero abscissa, their combination produces the described asymmetry, a consequence of the delayed strain response due to hysteresis when the uniaxial load on the specimen goes from tension to compression and vice-versa, changing the material elastic modulus. The fact that a single identified phenomenon in the experimental results can be simulated through the combination of two independently identified material models provides further evidence of their correct deduction.

Through the experimental data calculation, it was also possible to obtain the results reported in Table 3. If R4550 were a linear-elastic material, it should be expected that, once regime was achieved, the laser would be measuring around  $48\mu\text{m}$  of displacement amplitude with the zero abscissa as axis of symmetry, as demonstrated in Fig. 7. However, Table 3 reports that the laser signal is characterized by the same behaviour noticed in Fig. 6, where the displacement curves seem to progressively translate downwards as the amplitudes increase. Accordingly, the absolute value for minimum displacement is considerably larger than that of maximum displacement, supporting the correct attribution of combined viscoelasticity and asymmetric tension-compression elastic moduli as material models for graphite R4550.

Even considering the asymmetry with respect to the zero abscissa, none of the tests have reached the regime amplitude, which is further confirmed by the test durations being all below 10ms. The fact that none of the tests has reached regime condition is expected, since it means that failure was achieved in a low number of cycles (at most 140), during the ramp, while many of the counted cycles were still producing low loading amplitudes on the specimen, as indicated by the displacement curve applied to the specimen in Fig. 4. Accordingly, the described experimental test is not considered a fatigue test, with fatigue damage

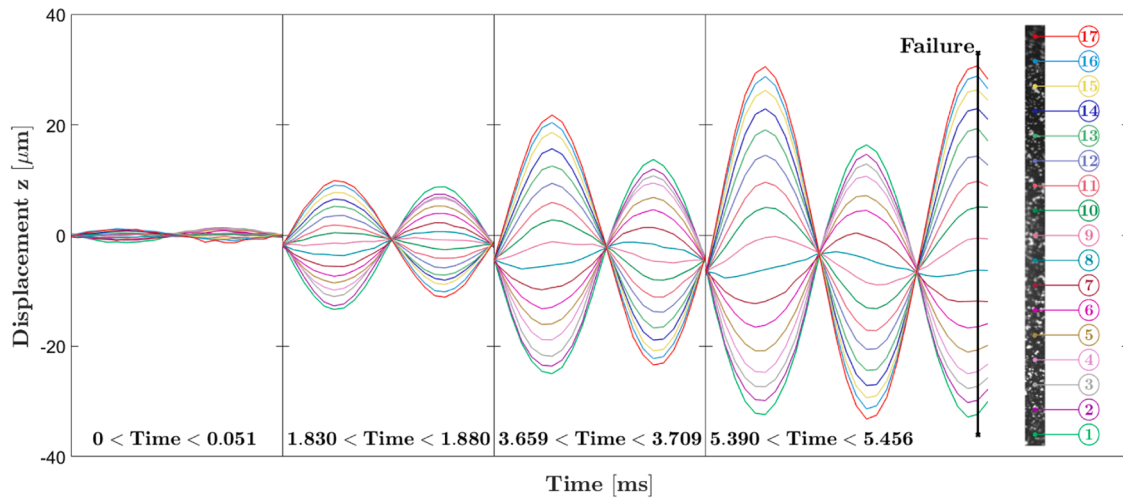


Fig. 6. Displacement results for graphite specimen 16 showing the amplitudes at different time ranges up to failure.

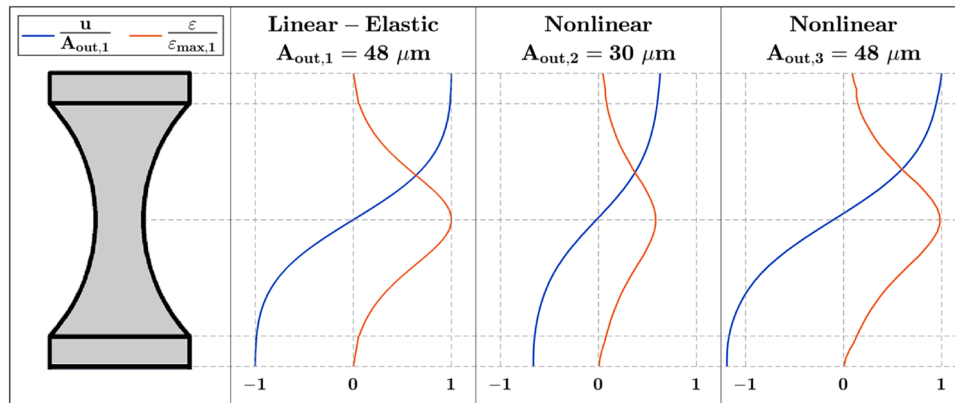


Fig. 7. Analytically calculated and normalized strain and displacement amplitudes for linear-elastic and nonlinear models of graphite hourglass specimens.

**Table 3**  
UST experimental results for graphite.

Specimen	Laser maximum [μm]	Laser minimum [μm]	Number of cycles	Test duration [ms]	Achieved $A_{out}$ [μm]
1	22.9	-36.1	110	5.4	32.7
2	26.8	-42.5	140	6.9	42.5
3	21.5	-43.6	114	5.6	37.4
4	24.5	-42.1	138	6.8	42.4
5	24.1	-42.5	139	6.9	42.7
6	24.0	-37.8	116	5.7	38.2
7	23.2	-36.7	87	4.3	36.7
8	27.7	-41.9	124	6.1	39.1
9	29.1	-40.4	113	5.6	42.3
10	23.8	-37.4	128	6.3	39.7
11	25.4	-36.8	106	5.2	37.8
12	25.1	-34.4	113	5.6	36.2
13	25.3	-39.7	98	4.9	43.5
14	23.1	-33.7	103	5.1	35.3
15	23.8	-37.4	129	6.4	38.0
16	26.9	-37.4	111	5.5	39.0

mechanisms having a negligible effect. Thus, the UST test can be reliably employed to approximate the quasi-static strength values of brittle materials.

Finally, all 32 fracture surfaces were observed on Field Emission Scanning Electron Microscopy (FESEM) to verify the presence of crack propagation region, i.e., fatigue damage mechanism. In all observations,

the fracture surfaces had the morphology shown in Fig. 8a, being impossible to determine where failure started or to identify its path, hence, suggesting no evidence of fatigue. Moreover, the microstructure of R4550 was also observed, in Fig. 8b, showing the usual morphology of isotatically pressed graphites, according to [64].

In Fig. 8b, there can be observed structures similar to those found in the analyses of fracture surface morphology of isostatic graphite for nuclear applications in [64], specifically:

- the flat and smooth surfaces resulting from filler particles that suffered trans-granular fracture (F);
- the rougher areas generated through intergranular fracture, corresponding to either pure binding carbon or binding carbon attached to filler particles that were not split during fracture (B);
- the voids that were produced during manufacturing or due to the dislodging of filler particles during failure (V).

The main difference between the graphite R4550 used in this work and the isostatic graphite in [64] (SNG623) is the grain size, considerably smaller for R4550, with the exposed filler particles at around  $10\mu\text{m}$ , while measuring roughly  $25\mu\text{m}$  for SNG623. Nevertheless, this is an expected result, since R4550 is said to be amongst the finest grain isostatic graphites.

#### 4.2. FEM optimization

The material model considered to simulate graphite R4550 me-



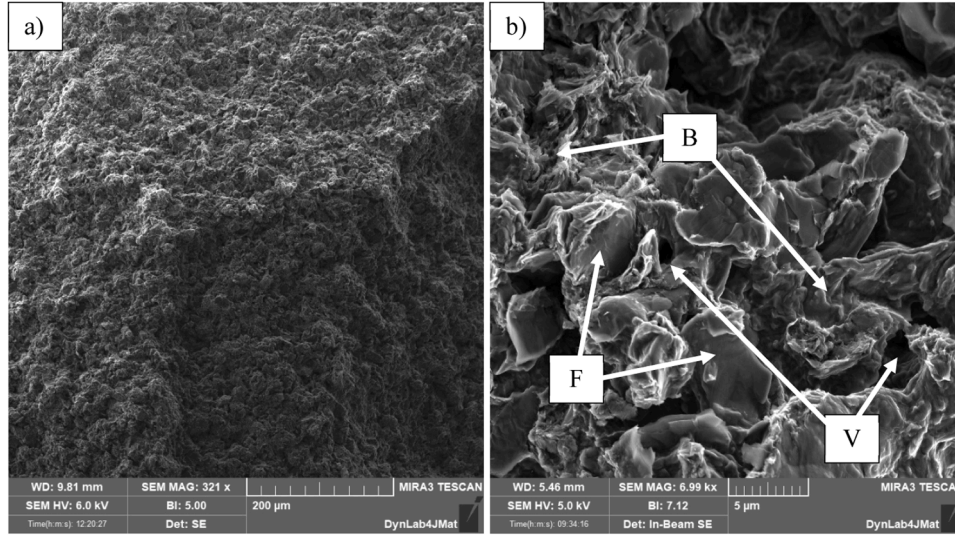


**Fig. 8.** FESEM images of graphite specimen fracture surfaces, illustrating (a) their general aspect, and (b) their microstructure indicating filler (F), binding carbon (B), and void (V).

chanical response should be able to replicate the out-of-phase behaviour of the experimental curves, the absence of a displacement node, the vertical translation of the supposed axis of symmetry, and the difference in elastic moduli in tension and compression. The two first-mentioned effects were immediately confirmed, through preliminary simulations, as being due to viscoelasticity [65–67], also identified in split Hopkinson pressure bar tests from [56], following the shear relaxation described by [68]:

$$G(t) = G_{\infty} + (G_0 - G_{\infty})e^{-\beta t} \quad (3)$$

being  $G$  the shear modulus at time  $t$ ,  $G_0$  the short-term or instantaneous shear modulus,  $G_{\infty}$  the long-term or infinite shear modulus, and  $\beta$  the decay constant. The delay caused by the relaxation can alter the phases in the same way as in Fig. 6, with the consequent disappearance of the displacement node.

However, the model described by Eq. (3) alone is not capable of replicating graphite asymmetrical behaviour in tension and compression. For this reason, a visco-hyperelastic model was considered [69], with hyperelasticity having as defining features the increase in elastic modulus during compression, and its decrease during tension, also proving to be effective for compressed expanded graphite [58] and for graphene [70,71]. Nevertheless, these changes only occur in these literature models once high strains are reached, i.e., above 10%, both for tension and compression, according to [72]. However, this is not the case of the investigated graphite, whose largest strains roughly estimated through the tracker results are between 0.5% and 1%.

For a proper simulation of this effect at low strains, a material allowing the setup of linear elasticity with two elastic moduli, one for tension ( $E_t$ ) and one for compression ( $E_c$ ), was chosen. For continuity purposes, the transition from  $E_t$  to  $E_c$  occurs when the stress changes from tensile to compression, or vice-versa. The resulting FE model, considering both viscoelasticity and asymmetric tension-compression behaviour, produces the stress-strain curve in Fig. 9, which represents the central cross-section of the specimen throughout the ramp, with the last cycle highlighted in red with  $A_{out}$  reaching  $48\mu\text{m}$ .

The model in Fig. 9 considers the viscoelasticity effect through the setup of values for  $\beta$ , and  $(G_0 - G_{\infty})$ , referred to as the shear relaxation modulus ( $G_1$ ), as required by the software LS-DYNA. Hence, the experimental behaviour can be successfully simulated through the optimization of 4 variables:  $E_t$  and  $E_c$ , from the linear-elastic part of the model, and  $G_1$  and  $\beta$ , to reproduce the hysteresis caused by viscoelasticity. The LS-OPT starting values and ranges for these 4 variables are reported in

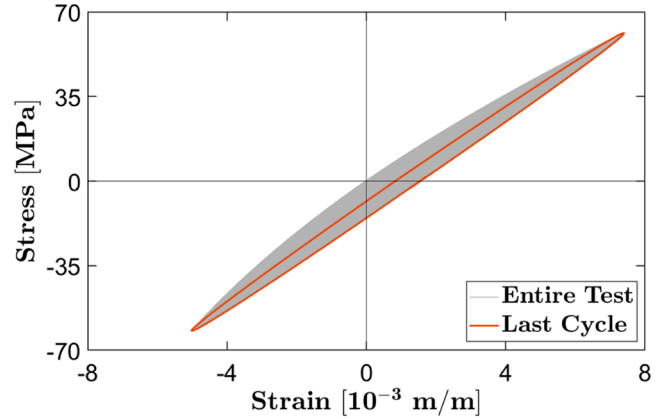


**Fig. 9.** Stress-strain curve for the central cross-section of the specimen applying the adopted nonlinear model to the UST test.

**Table 4**

Starting values and ranges for the optimization variables in LS-OPT.

Variable	Starting	Minimum	Maximum
Elastic modulus tension ( $E_t$ ) [GPa]	11.3	10.2	12.0
Elastic modulus compression ( $E_c$ ) [GPa]	11.7	10.4	12.2
Shear relaxation modulus ( $G_1$ ) [GPa]	1.2	0.0	2.4
Decay constant ( $\beta$ ) [ $\text{ms}^{-1}$ ]	40.0	0.0	80.0

**Table 4.** Particularly, the elastic moduli ranges are set considering the value of  $11.8\text{GPa}$  measured through IET in this work, and the fact that literature experimental data shows a slight reduction in the elastic modulus of graphite R4550 with the increase in strain during quasi-static tests [63]. However, since no optimized values for the viscoelastic parameters were found in the literature, the non-optimized values reported in [56], being  $G_1 = 1.22\text{GPa}$  and  $\beta = 40\text{ms}^{-1}$ , were set as starting values, with their respective ranges at  $\pm 100\%$  of them. The large ranges of the two latter variables take advantage of the domain reduction strategy adopted in LS-OPT, which consists of restricting the ranges of selectable values for the subsequent iteration according to results obtained in previous iterations, while also analysing all possibilities of convergence points.

Meanwhile, the density value was defined as the one measured from

the specimens, as in Table 1, and the Poisson ratio was used as 0.16, according to the literature on graphite R4550 [56], since it does not significantly affect the results for uniaxial displacements, consequently making its optimization through the collected experimental data ineffective. Finally, as optimization objectives, the displacement values measured through the tracker and the laser were used, with the optimization aiming to reduce the errors between the numerical and experimental displacements, as explained in SubSection 4.2.

Furthermore, not all the curves represented in Fig. 6 were utilized as optimization objectives. After excluding the tracker points whose measurements were considered non-valid, only a few of the larger amplitude curves were considered. There were two reasons for this choice: i) the reduction of percent error by avoiding the curves measuring lower amplitudes; and ii) to verify the optimization convergence capability by aiming to measure a large determination coefficient for all the valid displacement curves, despite not all data being used as optimization objective.

Since the elastic moduli seemed to converge faster and have a narrower range throughout the specimens, after running the first round of optimizations, the average of the converged values for  $E_t$  and  $E_c$  amongst all specimens were calculated and defined as fixed parameters. A new optimization round was then conducted having as variables only  $G_1$  and  $\beta$ , at the end of which  $G_1$  was averaged and fixed, with a final optimization round being conducted only on  $\beta$ , which was finally averaged amongst all specimens like the other variables. Considering the low availability of viscoelastic properties data on graphite R4550, this optimization sequence focused on converging the values of  $G_1$  and  $\beta$ .

#### 4.3. Optimized results

Once the final material properties were assessed as described in SubSection 4.2, the experimental displacements can be compared to the numerical ones calculated through the simulation on LS-DYNA using the converged material parameters for  $E_t$ ,  $E_c$ ,  $G_1$  and  $\beta$ . Fig. 10 shows the comparison between these displacements for specimen 16. The selected material model and the optimized properties are capable of reliably replicating graphite R4550 behaviour in the UST test, properly simulating the tension-compression asymmetry and viscoelasticity.

The properties resulting from the experimental tests and the following optimization process for graphite R4550 are reported in Table 5. The elastic moduli are 4.2% and 3.2% smaller, for tension and compression, respectively, than the dynamic elastic modulus obtained

**Table 5**

Graphite R4550 material properties.

Property	Value
Density [ $\text{kg/m}^3$ ]	1830
Elastic modulus tension ( $E_t$ ) [GPa]	11.31
Elastic modulus compression ( $E_c$ ) [GPa]	11.42
Shear relaxation modulus ( $G_1$ ) [GPa]	1.83
Decay constant ( $\beta$ ) [ $\text{ms}^{-1}$ ]	31.38

with the IET (equal to 11.8GPa), as expected given the nonlinearities concerning graphite behaviour. Moreover, these results are in agreement with literature data, suggesting the slight reduction in elastic modulus ( $E$ ) with the increase in strain, as observed in four-point bending tests from [63], work which also provided experimental data from IET, resulting in  $E = 11.5\text{GPa}$ .

Furthermore, the results in Table 5 can be compared to the numerical results obtained by simulating split Hopkinson pressure bar tests on R4550 [10], which considered a viscoelastic material, having  $E = 11.5\text{GPa}$ ,  $G_1 = 1.22\text{GPa}$ , and  $\beta = 40\text{ms}^{-1}$ . The shear relaxation modulus and decay constant values in [56] and in the present work show quite large differences. This can be explained by considering that in [56] no parameter optimization seems to have been carried out, with the model being purely viscoelastic and not considering graphite asymmetric tension-compression behaviour.

Additionally, the values  $G_1 = 1.22\text{GPa}$ , and  $\beta = 40\text{ms}^{-1}$  from [56] were applied to the material model in this work in conjunction with the optimized values of  $E_t$  and  $E_c$  reported in Table 5. This tentative simulation aimed to evaluate the capability of the viscoelastic parameters for graphite R4550 adopted in [56] to fit the experimental results from the UST test, with the results for specimen 16 being presented in Fig. 11. However, it is apparent that the numerical displacements obtained in the simulation with the viscoelastic parameters from [56] did not manage to reproduce the experimental displacements from the UST test as well as the simulation presented in Fig. 10, which used the values for  $G_1$  and  $\beta$  obtained in the present paper. Particularly, the viscoelastic parameters from [56] cannot properly simulate the compression stages of the UST test, providing evidence of the proper optimization of these parameters in the present work.

Hence, employing the optimized parameters from Table 5, Table 6 summarizes the estimated test results for each specimen. The coefficients of determination were calculated from the experimental and numerical displacement curves for the laser and the valid tracker points,

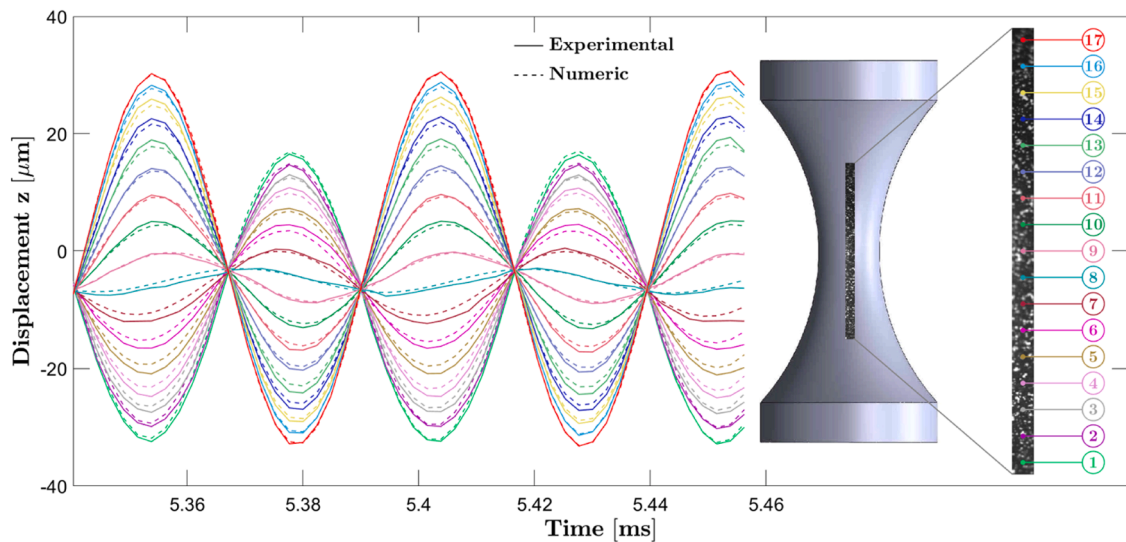


**Fig. 10.** Comparison between the experimental displacement curves calculated through the tracker and those obtained through the numerical model for graphite specimen 16.

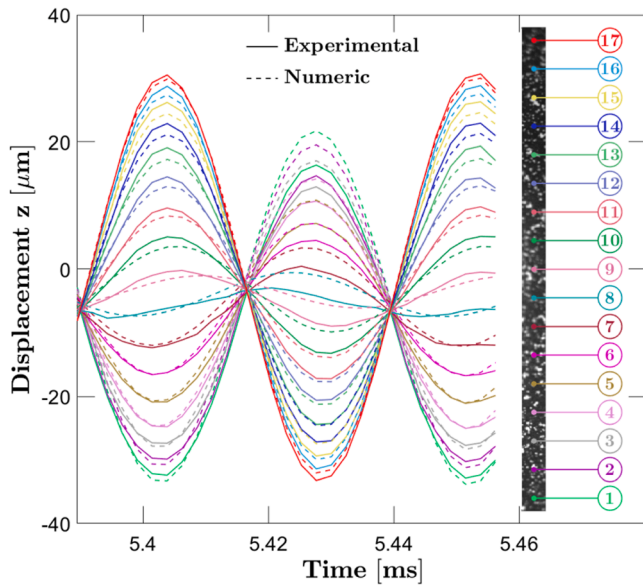


Fig. 11. Comparison between the numeric displacements applying the visco-elastic parameters from [56] and the experimental results for specimen 16.

Table 6

Summary of the results for the tested graphite specimens extracted from the optimized FE model.

Specimen	Average $R^2$	$\sigma_{max}$ [MPa]
1	0.937	50.5
2	0.984	59.6
3	0.984	57.8
4	0.988	59.6
5	0.978	60.3
6	0.994	53.5
7	0.994	51.7
8	0.968	55.1
9	0.988	59.7
10	0.990	55.9
11	0.995	53.0
12	0.993	51.0
13	0.986	61.3
14	0.985	49.7
15	0.992	53.4
16	0.995	55.0
Mean	0.984	55.4
Standard Deviation	0.014	3.7

all above 0.90, validating the chosen material model as well as the optimization process. Table 6 also reports the tensile strength, i.e., the maximum nominal tensile stress achieved in each specimen when failure happened, referred to as  $\sigma_{max}$ .

The calculated  $\sigma_{max}$  values for graphite R4550 are in accordance with values reported by suppliers, usually ranging from 40MPa to 60MPa, depending on the considered test method. Particularly, to further validate the experimentally assessed tensile strengths, they were compared to experimental values obtained through 4-point bending tests on graphite R4550 bars in [63], in which rectangular cross-section bars of 5mm height, 10mm width, and 25mm length have been tested (with 20mm span between supports, and a 10mm load span). The mean strengths for both tests, corresponding to 4-point bending ultimate strength and UST maximum tensile strength  $\sigma_{max}$ , are presented. Table 7 also reports the loaded volumes of the specimens tested in the present paper and in [63]. The loaded volume has been assumed as the material volume subjected to a stress above 90% of the maximum stress, providing an idea of the volume subjected to almost constant stress and at risk of crack nucleation [73].

Table 7

Comparison of strength data and loaded volumes for graphite submitted to UST test and 4-point bending.

Test configuration	Mean strength [MPa]	Loaded volume at $0.9 \cdot \sigma_{max}$ [mm <sup>3</sup> ]
UST	55.4	99.8
4-point bending	61.2	26.3

The results in Table 7 further confirm that the tensile strength values obtained through the UST test are in agreement with literature values for the investigated materials. Indeed, the differences with respect to 4-point bending experimental data can be attributed to size effect, according to [27,40], since the loaded volume in UST tests is considerably larger. Furthermore, the difference in testing configurations also affects the measured strength, with the stress gradient and the related size effect possibly having a significant influence [27]. It can be concluded that the difference is within the variability typical for brittle materials, thus validating the UST testing methodology.

As a final consideration, the specimens designed for these experimental tests did not focus on increasing the loaded material volume, despite still being larger than most loaded volumes employed in 3 and 4-point bending tests. However, since the UST tests were successfully executed in all 16 specimens in a small number of cycles with the set machine regime output being only 40% of the maximum limit, the loaded volume in future designs have margin to be considerably increased, like in previous research on uniaxial VHCF tests [73], provided they fulfil the frequency and amplitude constraints established in SubSection 2.2.

## 5. Conclusions

This paper proposes a novel testing procedure for the experimental and numerical assessment of tensile mechanical properties of brittle materials. The entirety of the methodology is performed on graphite R4550, bringing forward the following conclusions:

- 1 The ultrasonic testing equipment commonly used for fatigue tests was exploited to experimentally assess the tensile strength and the mechanical properties of graphite R4550. Failures in the fixture region are avoided since the specimen is connected to the testing device through an adhesive butt-joint subjected to stress close to zero. Similarly, testing misalignments are avoided, since only one extremity of the specimen is connected to the machine while the other remains free.
- 2 Since the operating limit of the ultrasonic equipment is a displacement amplitude and not a load, it potentially allows testing of high-resistance brittle materials with considerably larger loaded volumes than those found in the literature and possible with conventional testing methods, e.g., bending tests. Accordingly, the ultrasonic tensile methodology has potential flexibility in increasing the material loaded volume for investigating size effect.
- 3 Even if the specimen is loaded with input sinusoidal displacement at 20kHz, it is designed to fail before the occurrence of fatigue damage, allowing the measurement of tensile strength values close to those of quasi-static tests. Indeed, the ultrasonic tensile tests on graphite R4550 have proven that fatigue damage can be considered negligible after several observations: all specimens failed in at most 140cycles; since failure occurred during ramp to reach the imposed displacement, the majority of the loading cycles are therefore at low-stress amplitude levels; the fracture surfaces observed through field emission electron microscope showed no visible fatigue marks.
- 4 During the tests, displacements were measured through data collected by a laser and a high-speed camera. Although a uniaxial alternated tension-compression stress is applied, all specimens failed under tension and close to the gauge section, as expected.



- 5 The experimental displacements are used as objectives for an optimization process based on finite element analyses, aiming to minimize the differences between the experimental and the numerical displacements by varying the material parameters. This procedure allowed to estimate graphite R4550 material properties, establishing a numerical material model with viscoelastic and asymmetrical tension-compression behaviour, and subsequently calculating the tensile strength of each specimen.
- 6 The selected material model and optimization method were validated by the high determination coefficients computed by considering the numerical and experimental displacements for all tests, despite the restricted data selection as optimization objectives, confirming the method's high convergence capability.
- 7 The developed numerical modelling method was able to find a convergence for the material mechanical properties. The elastic moduli calculated through the ultrasonic tensile test are coherent with the ones found in the literature for graphite R4550 and the values measured through impulse excitation technique in this work. Meanwhile, the values obtained for the shear relaxation modulus and the decay constant showed the same order of magnitude as non-optimized values reported in the literature.
- 8 The tensile strength has been found to be close to literature values and within the range indicated by graphite R4550 suppliers, with the small differences being ascribed to different test methods (such as four-point bending test) and the different loaded volume.

To conclude, the developed ultrasonic tensile test and data analysis procedure allowed the assessment of mechanical properties of graphite R4550, being potentially applicable to most brittle materials, representing a reliable experimental-numerical alternative methodology for evaluating their uniaxial quasi-static behaviour.

#### CRediT authorship contribution statement

**A.P. Pagnoncelli:** Conceptualization, Data curation, Formal analysis, Investigation, Methodology, Software, Validation, Visualization, Writing – original draft, Writing – review & editing. **D.S. Paolino:** Conceptualization, Resources, Supervision, Writing – review & editing. **L. Peroni:** Conceptualization, Methodology, Resources, Supervision, Writing – review & editing. **A. Tridello:** Conceptualization, Resources, Supervision, Writing – review & editing.

#### Declaration of Competing Interest

The authors declare that they have no known competing financial interests or personal relationships that could have appeared to influence the work reported in this paper.

#### Data availability

Data will be made available on request.

#### Acknowledgments

The research used the equipment of J-Tech and DYNLab Laboratory at Politecnico di Torino co-funded by POR FESR Piemonte 2014–2020.

#### References

- [1] ASTM C1273 – 18 - standard test method for tensile strength of monolithic advanced ceramics at ambient temperatures. ASTM Int 2019. <https://doi.org/10.1520/mnl10913m>.
- [2] Liu KC, Pih H, Voorhes D. Uniaxial tensile strain measurement for ceramic testing at elevated temperatures: requirements, problems, and solutions. *Int J High Technol Ceram* 1988;4.
- [3] Zhang Q, Zheng Y, Zhou F, Yu T. Fragmentations of alumina (Al<sub>2</sub>O<sub>3</sub>) and silicon carbide (SiC) under Quasi-static compression. *Int J Mech Sci* 2020;167. <https://doi.org/10.1016/j.ijmecsci.2019.105119>.
- [4] Li Z, Chen W, Hao H. Mechanical properties of carbon foams under quasi-static and dynamic loading. *Int J Mech Sci* 2019;161–2. <https://doi.org/10.1016/j.ijmecsci.2019.105039>.
- [5] Hou C, Jin X, Zhao L, Li P, Fan X. Analysis of tensile strength and fracture toughness of ZrB<sub>2</sub> – SiC ceramic from three-point bending samples with edge cracks. *Ceram Int* 2022;48(20):30078–85. <https://doi.org/10.1016/j.ceramint.2022.06.278>.
- [6] Liu G, et al. Inverse identification of tensile and compressive damage properties of graphite material based on a single four-point bending test. *J Nucl Mater* 2018;509: 445–53. <https://doi.org/10.1016/j.jnucmat.2018.07.022>.
- [7] Zi G, Kim J, Bazant ZP. Size effect on biaxial flexural strength of concrete. *ACI Mater J* 2014;111(3):319–26. <https://doi.org/10.14359/51686576>.
- [8] Schlacher J, et al. Strength of additive manufactured alumina. *J Eur Ceram Soc* 2020;40(14). <https://doi.org/10.1016/j.jeurceramsoc.2020.03.073>.
- [9] Li Y, Zhong C, Qin T, Wang M. Preparation and performance of CaO-MgO-SiO<sub>2</sub>-Al<sub>2</sub>O<sub>3</sub>-CaF<sub>2</sub> glass/Al<sub>2</sub>O<sub>3</sub> ceramic with high flexural strength. *J Non Cryst Solids* 2023;602. <https://doi.org/10.1016/j.jnoncrysol.2022.122088>.
- [10] Kwok K, Kiesel L, Frandsen HL, Søgaard M, Hendriksen PV. Strength characterization of tubular ceramic materials by flexure of semi-cylindrical specimens. *J Eur Ceram Soc* 2014;34(5):1423–32. <https://doi.org/10.1016/j.jeurceramsoc.2013.12.005>.
- [11] Salavati H, Mohammadi H, Alizadeh Y, Ayatollahi MR. 3D fracture behaviour of graphite specimens weakened by V- notches with end holes under mixed mode (I+II) loading. *Eng Fail Anal* 2019;104. <https://doi.org/10.1016/j.engfailanal.2019.06.050>.
- [12] Fett T, Rizzi G, Ernst E, Müller R, Oberacker R. A 3-balls-on-3-balls strength test for ceramic disks. *J Eur Ceram Soc* 2007;27(1):1–12. <https://doi.org/10.1016/j.jeurceramsoc.2006.02.033>.
- [13] Staudacher M, Supancic P, Lube T. The Ball-on-Ring-test: enhancing an analytical solution by numerical analysis for elastic deformation and small displacements. *J Eur Ceram Soc* 2023. <https://doi.org/10.1016/j.jeurceramsoc.2023.06.016>.
- [14] Serati M, Alehossein H, Williams DJ. Estimating the tensile strength of super hard brittle materials using truncated spheroidal specimens. *J Mech Phys Solids* 2015; 78. <https://doi.org/10.1016/j.jmps.2015.02.011>.
- [15] Ma L, Yari N, Wiercigroch M. Shear stress triggering brittle shear fracturing of rock-like materials. *Int J Mech Sci* 2018;146–7. <https://doi.org/10.1016/j.ijmecsci.2018.07.008>.
- [16] Shams G, Rivard P, Moradian O. Observation of fracture process zone and produced fracture surface roughness in granite under Brazilian splitting tests. *Theor Appl Fract Mech* 2022;125. <https://doi.org/10.1016/j.tafmec.2022.103680>.
- [17] Newton CD, Jeffs SP, Gale L, Pattison S, Bache MR. Determining the interlaminar tensile strength of a SiCf/SiC ceramic matrix composite through diametrical compression testing. *J Eur Ceram Soc* 2023;43(7). <https://doi.org/10.1016/j.jeurceramsoc.2022.11.014>.
- [18] Kida K, Koga J, Santos EC. Crack growth and splitting failure of silicon nitride ceramic balls under cyclic pressure loads. *Mech Mater* 2017;106. <https://doi.org/10.1016/j.mechmat.2017.01.004>.
- [19] Zhang X, Yi Y, Zhu H, Liu G, Sun L, Shi L. Measurement of tensile strength of nuclear graphite based on ring compression test. *J Nucl Mater* 2018;511:134–40. <https://doi.org/10.1016/j.jnucmat.2018.09.010>.
- [20] Berto F, Lazzarin P, Ayatollahi MR. Brittle fracture of sharp and blunt V-notches in isostatic graphite under pure compression loading. *Carbon N Y* 2013;63:101–16. <https://doi.org/10.1016/j.carbon.2013.06.045>.
- [21] Xu Y, Dai F, Du H. Experimental and numerical studies on compression-shear behaviors of brittle rocks subjected to combined static-dynamic loading. *Int J Mech Sci* 2020;175. <https://doi.org/10.1016/j.ijmecsci.2020.105520>.
- [22] Wereszczak AA, Jadaan OM, Lin H-T, Champoux GJ, Ryan DP. Hoop tensile strength testing of small diameter ceramic particles. *J Nucl Mater* 2007;361. <https://doi.org/10.1016/j.jnucmat.2006.11.013>.
- [23] Calaf-Chica J, Martínez-Peña J, Bravo Díez PM, Preciado Calzada M. Ring Hoop Tension Test for yield strength estimation: numerical analysis for a novel correlation method and applicability for mechanical testing of tubes and pipes. *Mech Mater* 2022;169. <https://doi.org/10.1016/j.mechmat.2022.104295>.
- [24] Dai YJ, Jin SL, Zhou R, Li YW, Harmuth H, Tschegg EK. Mixed-mode fracture behaviour of refractories with asymmetric wedge splitting test. Part II: experimental case study. *Ceram Int* 2022;48(14):19757–66. <https://doi.org/10.1016/j.ceramint.2022.03.244>.
- [25] D'almeida JRM, Monteiro SN. The Iosipescu test method as a method to evaluate the tensile strength of brittle materials. *Polym Test* 1999;18:407–14. [https://doi.org/10.1016/S0142-9418\(98\)00043-9](https://doi.org/10.1016/S0142-9418(98)00043-9).
- [26] Guerrero-Miguel DJ, Alvarez-Fernández MI, Prendes-Gero MB, González-Niecha C. Determination of uniaxial tensile strength of brittle materials using tubular samples. In: IOP conference series: earth and environmental science. 833; Sep. 2021. <https://doi.org/10.1088/1755-1315/833/1/012016>.
- [27] Pagnoncelli AP, Tridello A, Paolino DS. Static strength of brittle materials under multiaxial nonuniform stress states: a novel statistical model for assessing size effects. *Fatigue Fract Eng Mater Struct* 2021;44(4):997–1013. <https://doi.org/10.1111/ffe.13409>. Apr.
- [28] Ray S, Haque M, Rahman M, Sakib N, Al Rakib K. Experimental investigation and SVM-based prediction of compressive and splitting tensile strength of ceramic waste aggregate concrete. *J King Saud Univ - Eng Sci* 2021. <https://doi.org/10.1016/j.jksues.2021.08.010>.

- [29] Wang Z, Ma D, Suo T, Li Y, Manes A. Investigation into different numerical methods in predicting the response of aluminosilicate glass under quasi-static and impact loading conditions. *Int J Mech Sci* 2021;196. <https://doi.org/10.1016/j.ijmecsci.2021.106286>.
- [30] Jacobsen GM, Stone JD, Khalifa HE, Deck CP, Back CA. Investigation of the C-ring test for measuring hoop tensile strength of nuclear grade ceramic composites. *J Nucl Mater* 2014;452(1–3):125–32. <https://doi.org/10.1016/j.jnucmat.2014.05.002>.
- [31] Kondo S, Katoh Y, Snead LL. Concentric ring on ring test for unirradiated and irradiated miniature SiC specimens. *J Nucl Mater* 2011;417(1–3):406–10. <https://doi.org/10.1016/j.jnucmat.2010.12.083>.
- [32] Staudacher M, Lube T, Schlacher J, Supancic P. Comparison of biaxial strength measured with the Ball-on-Three-Balls- and the Ring-on-Ring-test. *Open Ceram* 2021;6. <https://doi.org/10.1016/j.oceram.2021.100101>.
- [33] Huang JY, Yuan JC, Zhu TT, Zhong T, Xu YF, Luo SN. Dynamic compressive strength of alumina ceramics. *Ceram Int* 2022;48. <https://doi.org/10.1016/j.ceramint.2022.08.196>.
- [34] Volkov G, Smirnov I. A probabilistic approach to evaluate dynamic and static strength of quasi-brittle materials through high-rate testing. *Int J Mech Sci* 2022;216. <https://doi.org/10.1016/j.ijmecsci.2021.106960>.
- [35] Sato Y, Matsubara Y. The fracture of a solid brittle bar due to impact bending. *Int J Mech Sci* 1974;16.
- [36] Zheng J, Li H, Hogan JD. Strain-rate-dependent tensile response of an alumina ceramic: experiments and modeling. *Int J Impact Eng* 2023;173. <https://doi.org/10.1016/j.ijimpeng.2022.104487>.
- [37] Deng YJ, Chen H, Chen XW, Yao Y. Dynamic failure behaviour analysis of TiB2-B4C ceramic composites by split Hopkinson pressure bar testing. *Ceram Int* 2021;47(15):22096–107. <https://doi.org/10.1016/j.ceramint.2021.04.231>.
- [38] Friedrich LF, Colpo B, Koteski LE, Vantadori S, Iturrioz I. A novel peridynamic approach for fracture analysis of quasi-brittle materials. *Int J Mech Sci* 2022;227. <https://doi.org/10.1016/j.ijmecsci.2022.107445>.
- [39] Triantafillou TC, Gibson LJ. Multiaxial failure criteria for brittle foams. *Int J Mech Sci* 1990;32(6):479–96.
- [40] Pagnoncelli AP, Tridello A, Paolino DS. Modelling size effects for static strength of brittle materials. *Mater Des* 2020;195. <https://doi.org/10.1016/j.matdes.2020.109052>. Oct.
- [41] Li Z, Wang KF, Wang BL, Li JE. Size effect on the punch performance of brittle porous ceramics: theoretical analysis and numerical simulation. *Int J Mech Sci* 2021;207. <https://doi.org/10.1016/j.ijmecsci.2021.106674>.
- [42] Samadi S, Jin S, Gruber D, Harmuth H. A comparison of two damage models for inverse identification of mode I fracture parameters : case study of a refractory ceramic. *Int J Mech Sci* 2021;197. <https://doi.org/10.1016/j.ijmecsci.2021.106345>.
- [43] Irwin GR. Analysis of stresses and strains near the end of a crack traversing a plate. *J Appl Mech* 1957;24(3):361–4. <https://doi.org/10.1115/1.4011547>.
- [44] Eggers F, Almeida JHS, Azevedo CB, Amico SC. Mechanical response of filament wound composite rings under tension and compression. *Polym Test* 2019;78. <https://doi.org/10.1016/j.polymertesting.2019.105951>.
- [45] Sidi A, Gruber D, Harmuth H, Jin S. Tensile creep measurements of ordinary ceramic refractories at service related loads including setup, creep law, testing and evaluation procedures. *Ceram Int* 2016;42(6):6791–9. <https://doi.org/10.1016/j.ceramint.2016.01.056>.
- [46] Zhao J, Yan C, Liu S, Zhang J, Li S, Yan Y. Effect of solid waste ceramic on uniaxial tensile properties and thin plate bending properties of polyvinyl alcohol engineered cementitious composite. *J Clean Prod* 2020;268. <https://doi.org/10.1016/j.jclepro.2020.122329>.
- [47] Dikova T, Vasilev T, Dolgov N. Failure of ceramic coatings on cast and selective laser melted Co-Cr dental alloys under tensile test: experiment and finite element analysis. *Eng Fail Anal* 2019;105. <https://doi.org/10.1016/j.engfailanal.2019.07.018>.
- [48] Mazars V, et al. Damage investigation and modeling of 3D woven ceramic matrix composites from X-ray tomography in-situ tensile tests. *Acta Mater* 2017;140. <https://doi.org/10.1016/j.actamat.2017.08.034>.
- [49] Bauer J, et al. Push-to-pull tensile testing of ultra-strong nanoscale ceramic – polymer composites made by additive manufacturing. *Extrem Mech Lett* 2015;3. <https://doi.org/10.1016/j.eml.2015.03.006>.
- [50] Callaway EB, Zok FW. Tensile response of unidirectional ceramic minicomposites. *J Mech Phys Solids* 2020;138. <https://doi.org/10.1016/j.jmps.2020.103903>.
- [51] Valandro LF, Cadore-rodrigues AC, Dapieve KS, Machry V, Kalil G, Pereira R. A brief review on fatigue test of ceramic and some related matters in dentistry. *J Mech Behav Biomed Mater* 2023;138. <https://doi.org/10.1016/j.jmbbm.2022.105607>.
- [52] Mozafari F, Thamburaja P, Srinivasa AR, Moslemi N. A rate independent inelasticity model with smooth transition for unifying low-cycle to high-cycle fatigue life prediction. *Int J Mech Sci* 2019;159. <https://doi.org/10.1016/j.ijmecsci.2019.05.017>.
- [53] Campbell AA, Wereszczak AA, Snead MA, Katoh Y. Understanding the effect of specimen size on the properties of fine-grain isotropic nuclear graphite for irradiation studies: mechanical properties. *J Nucl Mater* 2023;576. <https://doi.org/10.1016/j.jnucmat.2023.154263>.
- [54] Uythoven J, et al. Upgrades to the LHC injection and beam dumping systems for the HL-LHC project. *IPAC14* 2015.
- [55] Garcia IL, et al. LHC injection protection devices, thermo-mechanical studies through the design phase. *IPAC2016* 2016:3698–701.
- [56] Peroni L, Scapin M, Carra F, Mariani N. Investigation of dynamic fracture behavior of graphite. *Key Eng Mater* 2013. <https://doi.org/10.4028/www.scientific.net/KEM.569-570.103>.
- [57] Vinod S, et al. Strain rate dependent shear plasticity in graphite oxide. *Nano Lett* 2016;16(2):1127–31. <https://doi.org/10.1021/acs.nanolett.5b04346>.
- [58] Jaszak P. Modeling of the elastic properties of compressed expanded graphite - a material used in spiral wound gaskets. *Int J Press Vessel Pip* 2020;187. <https://doi.org/10.1016/j.ijpvp.2020.104158>. Nov.
- [59] Alzoubi MF, Khateeb S, Al-Hallaj S. Modeling of compression curves of phase change graphite composites using Maxwell and Kelvin models. *J Compos Mater* 2016;50(8):1123–35. <https://doi.org/10.1177/0021998315588624>. Apr.
- [60] Tridello A, Paolino DS, Chianidussi G, Rossetto M. Gaussian specimens for VHCF tests: analytical prediction of damping effects. *Int J Fatigue* 2016;83. <https://doi.org/10.1016/j.ijfatigue.2015.04.025>. May.
- [61] Trško L, Nový F, Bokůvka O, Jambor M. Ultrasonic fatigue testing in the tension-compression mode. *J Vis Exp* 2018;(133):1–10. <https://doi.org/10.3791/57007>.
- [62] Costa PR, Montalvão D, Freitas M, Baxter R, Reis L. Cruciform specimens' experimental analysis in ultrasonic fatigue testing. *Fatigue Fract Eng Mater Struct* 2019;42(11):2496–508. <https://doi.org/10.1111/ffe.13041>.
- [63] Guardia Valenzuela J. Optimisation graphite-matrix composites for collimators in the LHC upgrade. *Universidad Zaragoza*; 2019.
- [64] März B, et al. Mesoscopic structure features in synthetic graphite. *Mater Des* 2018;142:268–78. <https://doi.org/10.1016/j.matdes.2018.01.038>. Mar.
- [65] Tayeb A, Arfaoui M, Zine A, Hamdi A, Benabdallah J. On the nonlinear viscoelastic behavior of rubber-like materials: constitutive description and identification. *Int J Mech Sci* 2017;130. <https://doi.org/10.1016/j.ijmecsci.2017.06.032>.
- [66] Wu R, Xu R, Wang G. Multiscale viscoelastic analysis of FRP-strengthened concrete beams. *Int J Mech Sci* 2023;253. <https://doi.org/10.1016/j.ijmecsci.2023.108396>.
- [67] Yang C, Jin G, Liu Z, Wang X, Miao X. Vibration and damping analysis of thick sandwich cylindrical shells with a viscoelastic core under arbitrary boundary conditions. *Int J Mech Sci* 2015;92. <https://doi.org/10.1016/j.ijmecsci.2014.12.003>.
- [68] Herrmann LR, Peterson FE. A numerical procedure for viscoelastic stress analysis. In: *ICRPG Mechanical Behavior Working Group*; 1968.
- [69] Talebi S, Darjani H. A pseudo-strain energy density function for mechanical behavior modeling of visco-hyperelastic materials. *Int J Mech Sci* 2021;208. <https://doi.org/10.1016/j.ijmecsci.2021.106652>.
- [70] Redzematovic M, Kirane K. Homogenization of the Mooney-Rivlin coefficients of graphene-based soft sandwich nanocomposites. *Mech Soft Mater* 2021;3(1). <https://doi.org/10.1007/s42558-021-00036-9>. Dec.
- [71] Ghaffari R, Sauer RA. A new efficient hyperelastic finite element model for graphene and its application to carbon nanotubes and nanocomposites. *Finite Elem Anal Des* 2018;146. <https://doi.org/10.1016/j.finela.2018.04.001>. Jul.
- [72] Ogden RW. Non-linear elastic deformations. Mineola, New York, USA: Ellis Horwood Ltd; 1984. <https://doi.org/10.1002/zamm.19850650903>.
- [73] Tridello A, Paolino DS, Rossetto M. Ultrasonic VHCF tests on very large specimens with risk-volume up to 5000mm<sup>3</sup>. *Appl Sci* 2020;10(7). <https://doi.org/10.3390/app10072210>. Apr.